Sustainable Energy & Fuels

ROYAL SOCIETY OF CHEMISTRY

PAPER

View Article Online
View Journal | View Issue

Cite this: *Sustainable Energy Fuels*, 2023, 7, 4618

Unravelling the role of iron carbide in oxygen reduction catalysts for rechargeable zinc–air batteries: a comprehensive kinetics & mechanistic study†

S. Arya Gopal, Anook Nazer Eledath and Azhagumuthu Muthukrishnan *

Rechargeable metal–air batteries are an emerging electrochemical energy storage technology wherein the invention of bifunctional electrocatalysts for the oxygen reduction reaction (ORR) and oxygen evolution reaction (OER) plays a critical role in the device's performance. Recently, Fe_3C-based carbon materials have been reported for their excellent bifunctional activity. The lack of understanding in defining the role of Fe_3C impedes the design of high-performance catalysts. Fe_3C on carbon (Fe_3C/C) and Fe_3C on nitrogen-doped carbon (Fe_3C/NC) are synthesised using various carbon substrates. The mechanistic analysis from the rotating ring-disk electrode voltammogram demonstrates the formation of 4-electron active sites while introducing Fe_3C and nitrogen in the graphitic carbon substrate, and the reason for the superior ORR activity is discussed. The activity and stability are evaluated using a zinc–air battery experiment. Fe_3C & N-doped Vulcan carbon exhibits higher power density (167 mW cm^{-2}) and specific capacity (756 mA h g_{Zn}^{-1} @ 20 mA cm^{-2}). Besides, Fe_3C & N-doped Vulcan carbon shows excellent stability with 88% efficiency after 300 cycles (20 minutes per cycle) of continuous charge–discharge operation at a current density of 5 mA cm^{-2}. All the Fe_3C/NC catalysts show excellent stability in the OER region, and this study guides the futuristic design of Fe_3C-based catalysts for zinc–air battery electrodes.

Received 22nd May 2023
Accepted 7th August 2023

DOI: 10.1039/d3se00676j

rsc.li/sustainable-energy

1. Introduction

Developing platinum-free electrocatalysts for the oxygen reduction reaction (ORR) at cathodes of fuel cells and metal–air batteries is one of the paramount research studies in energy conversion and storage systems. Among the non-platinum group metal catalysts developed so far, Fe-containing N-doped carbon (Fe–N/C) materials are promising potential alternatives for state-of-the-art catalysts in terms of activity and durability. The activity of Fe–N/C can be tuned in many ways, such as by using suitable precursors, pyrolysis temperature, time, atmosphere, *etc.* The real active sites of Fe–N/C catalysts remain unsolved despite various theories proposed depicting different active sites for O_2 adsorption.[1–12] Though the Fe content is very low (traces to 3 wt%) in most of the Fe–N/C catalysts, it was believed that Fe–N_x active sites are responsible for the superior ORR activity. Besides Fe–N_x, multitudinous iron-containing compounds were found in Fe–N/C catalysts, such as oxides, carbides, encapsulated iron nanoparticles, *etc.* It is essential to study the role of individual components in Fe–N/C catalysts to understand real active sites, which helps in designing very active and highly durable electrocatalysts for the ORR.

Iron carbides are the frequently encountered species in heat-treated Fe–N/C catalysts. It is well-known that heating carbon with iron precursors at higher temperatures (>700 °C) generates iron carbides.[13–16] Hence the formation of iron carbide is inevitable in the process of Fe–N/C synthesis *via* the pyrolysis of organic precursors in an inert atmosphere. The synthesis of Fe_3C from various precursors and their ORR activity were reported elsewhere.[15,17–26] Nevertheless, most reported materials were synthesised from Fe and nitrogen-containing precursors and denoted as Fe_3C@N–C, Fe@Fe_3C/Fe–N_x, Fe_3C/Fe–N_x, *etc.* In these catalysts, the origin of the ORR activity is not only from the Fe_3C sites but also from the Fe–N_x and N–C active sites formed during the process. The ORR activity and mechanism of Fe_3C (without nitrogen precursors) on carbon supports were not analysed in the literature. The role of Fe_3C can be demonstrated only in the absence of any other heteroatoms, particularly the absence of Fe–N_x active sites.

Fe_3C/Fe–N_x or Fe–Fe_3C encapsulated N-doped carbon materials were studied, and their improved ORR activity was observed in the literature. The reason for the improved activity was explained by the synergistic effect of the encapsulated Fe_3C

School of Chemistry, Indian Institute of Science Education Research Thiruvananthapuram, Maruthamala P.O., Vithura 695 551, Kerala, India. E-mail: muthukrishnan@iisertvm.ac.in

† Electronic supplementary information (ESI) available. See DOI: https://doi.org/10.1039/d3se00676j

with Fe–N_x or N–C active sites.[14,27–33] In the case of Fe_3C/Fe–N_x composites, the relative content of each species determines the mechanistic pathway. Fe–N_x promotes the $4e^-$ direct pathway whereas Fe_3C directs the reduction *via* the stepwise pathway (2 + 2e ORR).[34,35] The N-doped carbon encapsulated Fe_3C nanoparticles are active towards the oxygen evolution reaction (OER), whereas Fe–N_x or N–C active sites are known for the ORR. Hence the dual active sites of Fe_3C/Fe–N_x composites act as a bifunctional catalyst in Zn–air batteries.[19,30,36,37] It was also believed that the formation of Fe_3C suppresses the formation of Fe–N_x active sites, which is mandatory for the ORR. Thus, the formation of Fe_3C (2-electron active sites) was suppressed by adding sulphur, which enhanced Fe–N_x sites.[38] The theoretical analysis indicates that Fe_3C enhances the ORR activity by minimising the adsorption activation energy. However, the ORR kinetics limited by the strongly adsorbed intermediates, especially the reductive desorption of *OH from the active sites, is not thermodynamically favoured.[13]

Herein, the role of Fe_3C present in heat-treated Fe–N/C catalysts is demonstrated using pure Fe_3C on various carbon supports with different porosities. The encapsulated or Fe_3C-supported carbon materials are studied using RRDE voltammetry, and their role in the ORR is defined by analysing the mechanism using kinetic parameters. The Fe_3C encapsulated or Fe_3C supported by N-doped carbon materials is also studied to understand the role of each active site (Fe_3C, Fe–N and N–C) towards the ORR. The zinc–air battery testing demonstrates excellent OER performance for longer cycles, revealing the dual active site concepts for the OER and ORR in Fe_3C-containing N-doped carbon catalysts. The role of carbon supports is also discussed elaborately.

2. Methodology

2.1 Synthesis of Fe_3C/C and Fe_3C/NC composites

The synthesis of Fe_3C on carbon materials was explained as shown in Fig. 1. Briefly, the conductive carbon (Ketjen black EC300J (KB) or Vulcan carbon XC-72 (VC) or graphene oxide (GO)) was uniformly dispersed in 0.1 M $Fe(NO_3)_3 \cdot 9H_2O$ solution, followed by the slow addition of 0.05 M $K_4(Fe(CN)_6)$ to form a carbon–Prussian blue (PB) composite. The precipitate was washed with DI water and dried. The carbon–PB composite was transferred into an alumina boat and kept in a tube furnace. The furnace was heated at a rate of 5 °C min^{-1} under a flow of N_2 (flow rate: 40 mL min^{-1}) and was kept at 900 °C for 2 hours before cooling to room temperature naturally. Finally, the samples were collected from the furnace and washed with 0.1 M HCl to remove excess iron species from the material. Thus the synthesised material is referred to as Fe_3C/C (C refers to KB or VC or rGO). The heat-treated (900 °C) bare carbon substrates (synthesised using a similar method adopted for Fe_3C/C) were employed as control samples to study the role of Fe_3C. Previously, the carbon samples (KB and VC) were washed with 1 M HCl solution to remove metal impurities, whereas GO was synthesized using a modified Hummers' method, as reported earlier.[39]

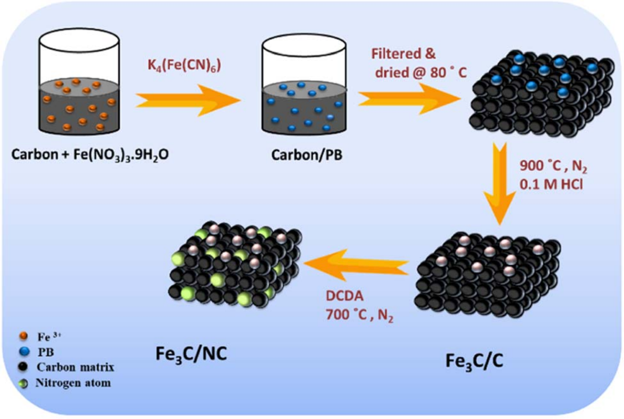

Fig. 1 Schematic representation of the synthetic methods of Fe_3C/C and Fe_3C/NC materials.

The Fe_3C/NC materials were synthesised from a mixture of previously synthesised Fe_3C/C and dicyandiamide (DCDA) in a ratio of 1 : 10. The mixture was transferred to an alumina boat and heated at 700 °C with a ramp rate of 3 °C min^{-1} (other conditions are very similar to those in the procedure described above). Thus the synthesised material is referred to as N-doped Fe_3C/carbon (Fe_3C/NC) catalysts.

Pure Fe_3C was synthesized by the thermal decomposition of Prussian blue (PB) at higher temperatures. An aqueous solution of 0.1 M $Fe(NO_3)_3 \cdot 9H_2O$ was mixed with 0.05 M $K_4(Fe(CN)_6)$ with constant stirring, producing a blue colour precipitate of PB. The PB was filtered and washed with ethanol and water. The vacuum-dried PB was heated to 900 °C under similar conditions described above to get Fe_3C. The formation of pure Fe_3C was further confirmed by X-ray diffraction spectroscopy.

2.2 Electrochemistry

The electrochemical studies were performed using a PARSTAT multichannel potentiostat in a custom-made electrochemical cell (200 ml). The linear sweep hydrodynamic voltammetric technique was employed using a rotating ring-disk electrode (RRDE, PINE Instruments) in O_2-saturated 0.1 M KOH electrolyte. The RRDE consists of a glassy carbon (GC) disk (5.6 mm diameter) and a Pt ring electrode with a theoretical collection efficiency of 0.37. The GC disk of the RRDE was modified with the catalysts as given below. The catalytic ink was prepared by weighing 5 mg of the catalysts (Fe_3C or Fe_3C/C or Fe_3C/NC or N–C) with isopropanol (0.15 ml), Type 1 water (0.15 ml) and a Nafion® (0.05 ml of 5 wt%) binder.[40,41] The catalyst ink was made by dispersing the above mixture using a sonicator. A known amount of the ink was taken using a micropipette and drop-coated on the GC disk of the RRDE, maintaining a loading density of 200 μg cm^{-2}. The catalyst-modified GC disk, carbon cloth with a graphite rod and Ag/AgCl (sat. KCl) were used as working, counter and reference electrodes, respectively. All the potentials were corrected against a reversible hydrogen electrode (RHE) using the pH of the electrolyte. Blank experiments in N_2-saturated electrolytes were performed to measure the background charging current. The disk electrode was scanned linearly from 1 V to 0 V at a scan rate of 10 mV s^{-1}, whereas the ring electrode was kept at a constant potential of 1.2 V to estimate the H_2O_2 intermediate quantitatively. The stability of the catalysts was analysed using the accelerated durability test.[42] Briefly, the catalyst-coated GC rotating disk electrode (5 mm diameter) was scanned between 1.0 and 0.6 V at a scan rate of 100 mV s^{-1} for 10 000 cycles in an O_2-saturated 0.1 M KOH electrolyte. Linear sweep voltammetry before and after the durability cycles was performed at 1600 rpm rotational speed in O_2-saturated 0.1 M KOH electrolyte (scan rate is 10 mV s^{-1}).

3. Results and discussion

3.1 Characterisation

X-ray diffraction (XRD) spectroscopy (Bruker XRD, CuKα, λ = 1.5406 Å, 40 kV, 40 mA) was used to confirm the crystalline nature of the materials (Fe_3C and carbon). The diffraction patterns of pure Fe_3C nanoparticles (JCPDS No. 35-0772) have been compared with those of the synthesised composites.[20] All the synthesised materials (before the acid-washing step) show a characteristic peak at 45°, which corresponds to the bulk Fe particles (JCPDS-06-0696) formed along with the Fe_3C nanoparticles (Fig. S1†).[26] The acid-washed Fe_3C/C compounds exhibit a diffraction peak at 25.5° (002), which corresponds to the graphitic carbon. Only excess Fe_3C is removed during acid-washing, and the presence of Fe_3C is confirmed by the less intense peaks (Fig. 2a). The encapsulated Fe_3C or Fe nanoparticles present inside the micro and mesopores of the carbon matrix remain in the materials after acid washing. In the case of Fe_3C/NrGO, a small peak observed at 35° indicates the presence of iron oxides (Fe_2O_3), and later, it was confirmed by elemental mapping using transmission electron microscopy (TEM).

The quantitative estimation of Fe in Fe_3C or Fe_3C/NC was performed using the thermogravimetric analysis[43] (SDT-Q-600, TA Instruments). More accurate measurements using inductively coupled plasma optical emission spectroscopy (ICP-OES) result in a significant error due to the difficulty in sample preparation for ICP-OES (incomplete extraction of metal species using acids). The TGA experiment was performed under a flow of air. From the thermogravimetric curves, the weight loss observed above 450 °C (Fig. 2b) can be attributed to the oxidation of carbonaceous content. The TGA curves are parallel to the

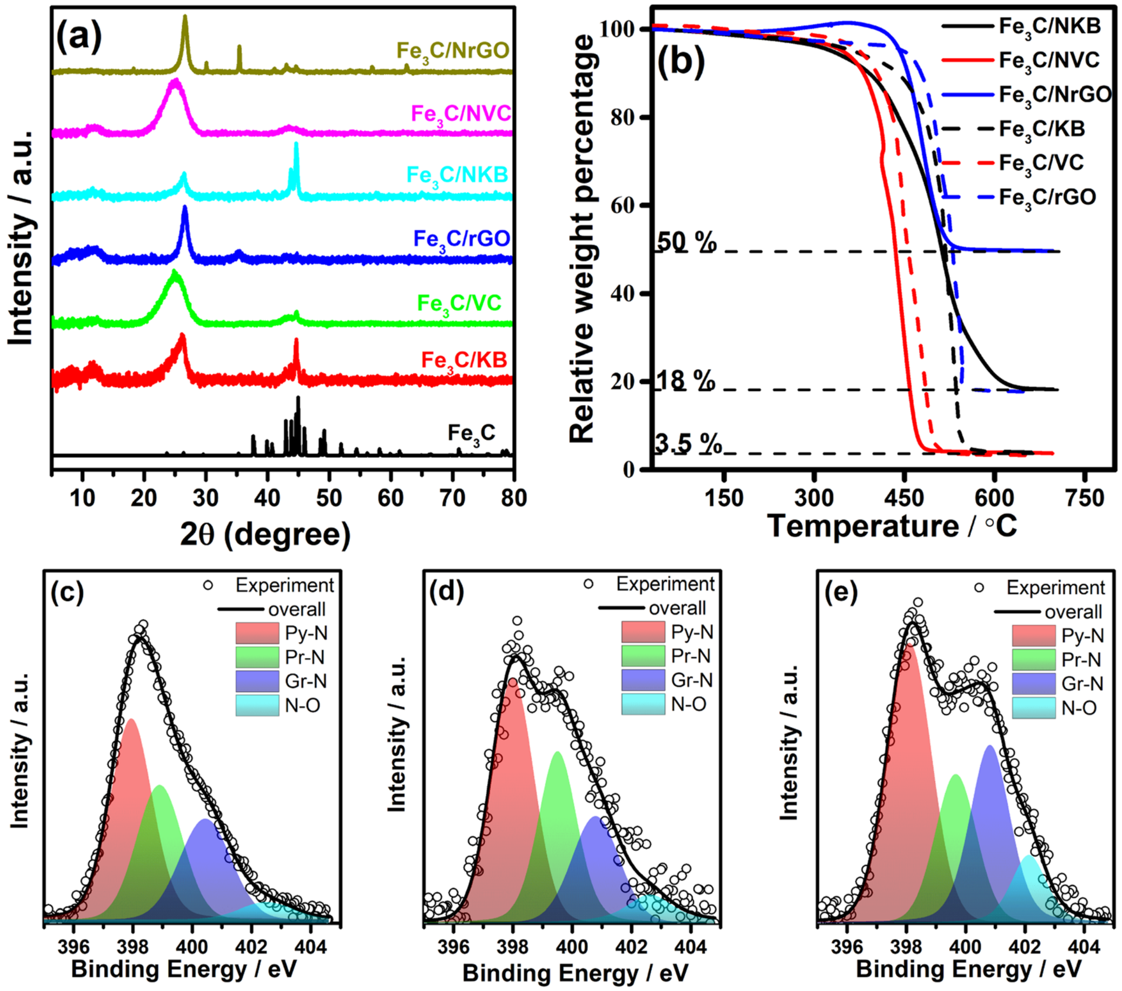

Fig. 2 (a) The powder XRD pattern of Fe_3C, Fe_3C/C and Fe_3C/NC composites. (b) TGA plots of Fe_3C/C and Fe_3C/NC composites to estimate the iron contents in the samples. N 1s XPS spectra of (c) Fe_3C/NKB, (d) Fe_3C/NVC and (e) Fe_3C/NrGO compounds and their components after deconvolution.

x-axis beyond 650 °C, indicating that all the carbon-based materials are burned out and the remaining must be the oxides of iron species. The powder XRD analysis reveals the formation of Fe_2O_3 after the removal of carbon content (Fig. S2†). The Fe content was calculated from Fe_2O_3, as shown in Table S1.† The higher Fe content in Fe_3C/rGO can be explained by the relatively significant carbon content loss of the carbon support (GO) compared with other carbon supports. The Fe content of Fe_3C/NVC retains its original values, whereas the Fe in Fe_3C/NKB and Fe_3C/NrGO increased to 3 times that of the Fe content in Fe_3C/C. This indicates that KB and rGO lose carbon content during the N-doping.

X-ray photoelectron spectroscopy (XPS) exhibits the elements in the materials and their chemical states. XPS experiments (Omicron Nanotech, excitation source: MgKα, kinetic energy: 1253.6 eV in constant analyser energy mode with a pass energy of 50 eV) were performed to investigate the bonding nature of the elements. The survey spectra of Fe_3C/C compounds indicate that the major component of the materials consists of carbon (Fig. S3†), wherein the C-1s peak was centred at 284.2 eV, corresponding to sp^2 carbon. The small pre-peak at 283.4 eV represents the carbon bonded with Fe (in Fe_3C). The deconvoluted peak from 286 to 288 eV indicates the carboxyl group (Fig. S4†). Fe is not seen in the survey spectra because of the carbon layers encapsulating Fe_3C, which makes it more difficult to detect the core Fe_3C. However, Fe_3C/NKB and Fe_3C/NrGO show less intense peaks at 708.6 eV ($2p_{3/2}$) and 721.7 eV ($2p_{1/2}$), corresponding to the Fe-2p XPS peaks (Fig. S5†). No Fe-2p peak was observed due to the lower Fe content in Fe_3C/NVC. Fig. 2c–e show the N-1s XPS spectra of Fe_3C/NC compounds, which were deconvoluted into four peaks corresponding to pyridinic, pyrrolic, and graphitic nitrogen and nitrogen oxides. The nitrogen content estimated from the XPS peaks is given in Table S1.† Due to the lower Fe content in Fe_3C/NVC, nitrogen doping is significantly reduced to 1.2 wt%. The majority of the nitrogen content is in the form of pyridinic nitrogen, known for its positive impact on the ORR activity.[7,44,45]

The surface area and pore size distribution were measured using N_2-sorption isotherms (Micrometrics 3Flex analyser), as shown in Fig. 3. The Fe_3C/C and Fe_3C/NC materials exhibit type IV adsorption isotherms with H3/H4 hysteresis loops. The Brunauer–Emmett–Teller (BET) surface area and the pore volume of the composite materials are listed in Table 1. Pure KB exhibits the highest surface area, followed by rGO and VC. BET surface area of the composites (Fe_3C/C) is smaller than the corresponding bare carbon support surface area, and it can be rationalised by filling pores (of the carbon support) with non-porous Fe_3C. The Fe_3C/C compounds before acid washing (Fe_3C/C(BAW)) show less surface area than Fe_3C/C (Fig. S6†), supporting the above statement. The substantial decrease in the surface area of Fe_3C/NC compared with Fe_3C/C can be explained as follows. A graphitic carbon layer was formed on the surface of porous carbon materials during the pyrolysis at a higher temperature. The subsequent reduction in the pore volume from bare carbon to Fe_3C/C to Fe_3C/NC validates the pore blocking by Fe_3C followed by the graphitisation. The non-linear density functional theory (NLDFT) modelling of pore size (Fig. S7†) indicates no significant changes in the pore size distribution of Fe_3C/KB and Fe_3C/VC from their corresponding carbon supports. However, rGO lost its micropores after the incorporation of Fe_3C followed by the N-doping. The pore size distribution curves of Fe_3C/NC show a decrease in micropores with the formation of meso and macropores. The decrease in the surface area in each step (carbon to Fe_3C/C to Fe_3C/NC) is less pronounced in VC composites[46] due to the low Fe content (corroborated by TGA analysis).

The morphology of the Fe_3C/C composites was analysed using high-resolution TEM images which demonstrate the presence of Fe_3C particles distributed on the carbon support (Fig. 4). The Fe_3C nanoparticles are encapsulated by the graphite layer (Fig. S9†), and Fe_3C particles were seen to be less than 50 nm in size. However, Fe_3C formed on rGO is larger in size as bulky particles. The selected area diffraction (SAED) pattern of Fe_3C/C indicates fringes with a *d*-spacing value of 0.24 and 0.2, corresponding to the 112 and 121 planes of Fe_3C.[29,47] The TEM images of Fe_3C/NC compounds indicate the presence of connected carbon particles with occasional nanotubes in Fe_3C/NKB, and more pictures are shown in Fig. S10.† The high-angle annular dark-field scanning transmission electron microscopic (HAADF-STEM) images clearly distinguish the

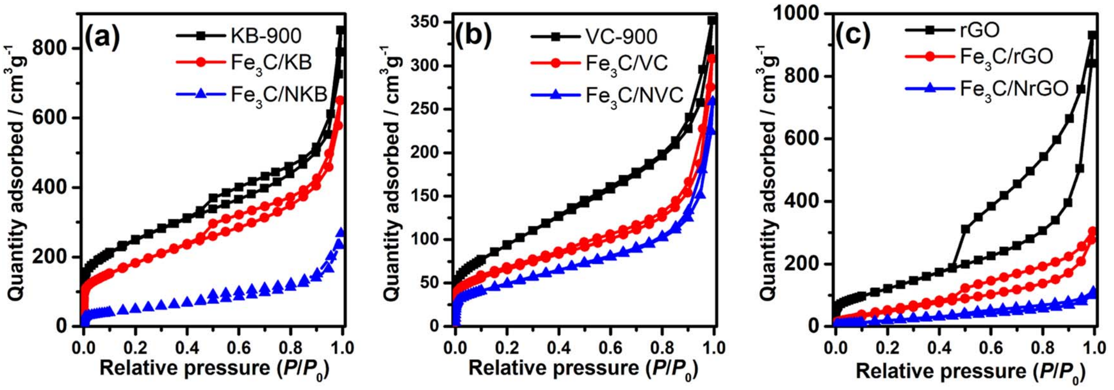

Fig. 3 The N_2-sorption isotherms of carbon supports (a) KB, (b) VC and (c) rGO before and after the incorporation of Fe_3C and Fe_3C followed by N-doping.

Table 1 Parameters obtained from the N_2-adsorption isotherm

Compound	S_{total} ($m^2 g^{-1}$)	$S_{micro}{}^a$ ($m^2 g^{-1}$)	$S_{meso}{}^b$ ($m^2 g^{-1}$)	$V_{total}{}^c$ ($cm^3 g^{-1}$)	$V_{micro}{}^d$ ($cm^3 g^{-1}$)	$V_{meso}{}^e$ ($cm^3 g^{-1}$)
KB-900	891	71.4	309.3	1.320	0.025	0.223
Fe_3C/KB	654	55.7	278.8	1.007	0.019	0.20
Fe_3C/NKB	155	—	107.6	0.416	—	0.080
VC-900	335	35.0	138.6	0.545	0.010	0.109
Fe_3C/VC	235	15.7	82.8	0.447	0.008	0.05
Fe_3C/NVC	157	—	71.2	0.400	—	0.058
rGO	430	6.2	489.4	1.442	0.012	0.450
Fe_3C/rGO	176	3.4	207.9	0.471	0.003	0.150
Fe_3C/NrGO	88	—	70.7	0.171	—	0.054

[a] Microporous surface area (S_{mic}). [b] Mesoporous surface area (S_{meso}) obtained from Barett–Joyner–Halenda (BJH) method. [c] Total pore volume. [d] Microporous volume (V_{mic}) obtained from the t-plot. [e] Mesoporous volume (V_{meso}).

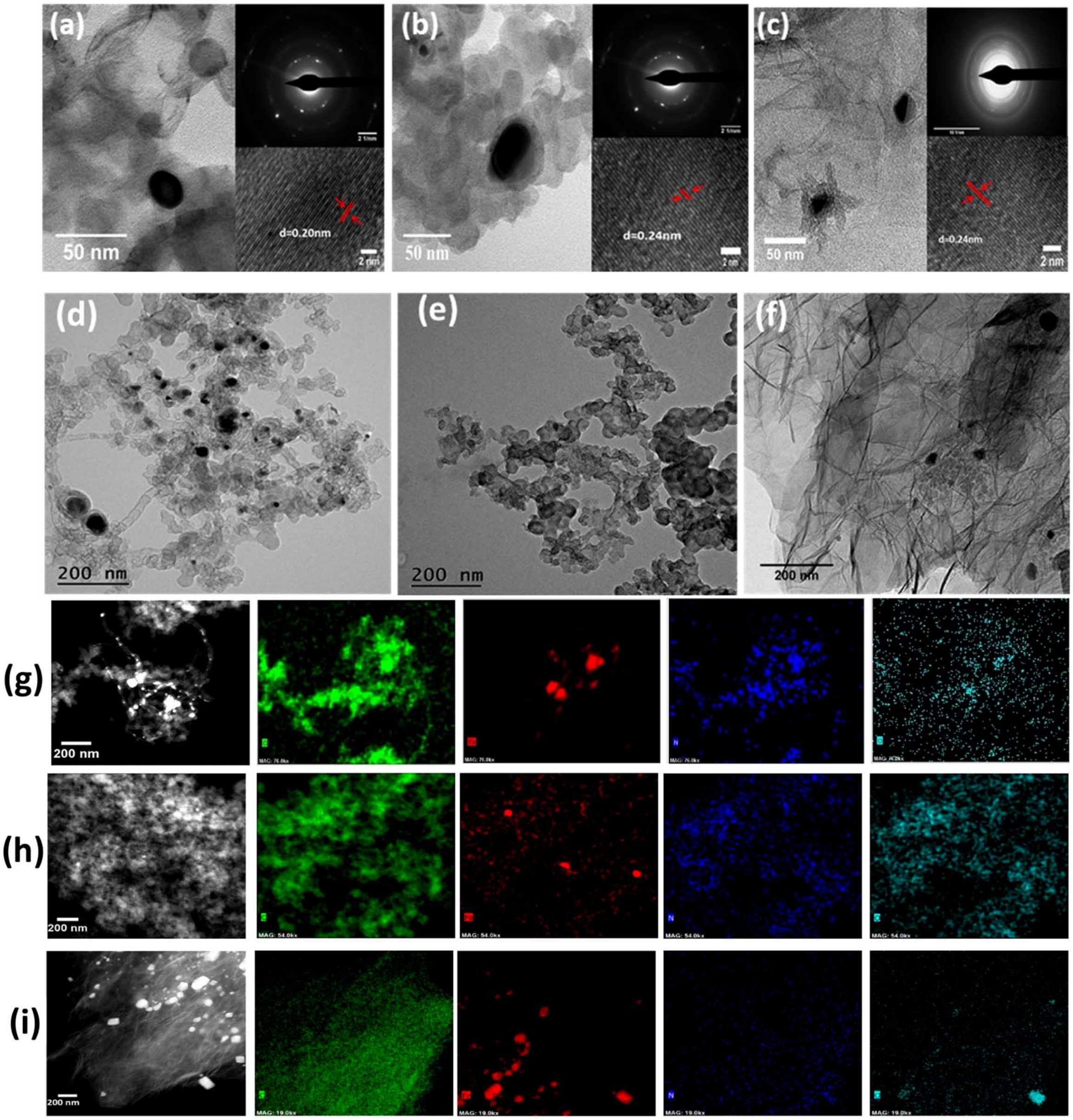

Fig. 4 High-resolution TEM images of Fe_3C/C (a–c) and Fe_3C/NC (d–f). From left to right: KB, VC and rGO supported Fe_3C with and without N-doped carbon. HAADF-STEM images and EELS elemental mapping of (g) Fe_3C/NKB, (h) Fe_3C/NVC, and (i) Fe_3C/NrGO. From left to right: HAADF-STEM images and carbon, iron, nitrogen and oxygen elemental mapping.

individual Fe_3C particles. The electron energy loss spectroscopy (EELS) elemental mapping confirms the presence of carbon, iron, nitrogen and oxygen distributed in the materials. Besides Fe_3C, the Fe_2O_3 formation is also confirmed based on overlapping the individual elemental mappings in the composites. However, other than Fe_3C/NrGO, the XRD cannot show any Fe_2O_3 peaks, as reported earlier.

3.2. Oxygen reduction reaction activity

Fig. 5a–c show RRDE voltammograms of the ORR on bare carbon, Fe_3C/C and Fe_3C/NC catalysts. The onset (E_{onset}) potential (kinetically controlled region), half-wave ($E_{1/2}$) potential (mixed kinetic-diffusion controlled region) and limiting current density (j_{DL}) (diffusion controlled region) are used as activity descriptors to compare the ORR activity (Table S4†). The bare carbon materials show a typical double sigmoidal curve, pertaining to the 2-electron ORR (O_2 to H_2O_2) at lower overpotentials (>0.4 V) and 2 + 2-electron ORR (O_2 to H_2O *via* H_2O_2) at higher overpotentials (<0.4 V). The number of electrons (*n*) is estimated using ring and disk currents (see the ESI†), which is close to 2, corroborating the 2-electron ORR. However, it is increasing to 3 and above on bare KB and VC compounds at larger overpotentials (Fig. 5f) due to H_2O_2 reduction catalysed by narrow micropores (<0.7 nm).[48] In rGO, the *n* value is almost constant throughout the applied potential due to the negligible number of narrow micropores (Section 3.1). The introduction of Fe_3C in the carbon materials exhibits improved E_{onset} and $E_{1/2}$ and j_{DL}, indicating a positive impact of Fe_3C on the ORR activity. The positive shift in E_{onset} and $E_{1/2}$ is more pronounced in Fe_3C/NC than in Fe_3C/C. The E_{onset} values are 0.96 (Fe_3C/NKB), 0.90 (Fe_3C/NVC) and 0.95 V (Fe_3C/NrGO), which are 70, 50 and 30 mV more positive than those of Fe_3C/KB, Fe_3C/VC and Fe_3C/rGO, respectively. Similarly, $E_{1/2}$ values show a positive shift and the limiting current improved in Fe_3C/NC materials. Besides, a well-defined mass transport-controlled limiting region was observed with smaller ring currents. The *n* values are increased for Fe_3C/NC catalysts compared with Fe_3C/C catalysts (Fig. 5d and e). The *n* value of Fe_3C/NKB and Fe_3C/NVC compounds is 3.9, indicating the complete reduction of O_2 to H_2O. The RRDE voltammograms of Fe_3C/C, Fe_3C/NC, NC and only carbon supports at various rotational speeds are given in Fig. S11.†

Nitrogen-doped carbon materials were prepared without Fe_3C to study the role of Fe_3C. The ORR activity of N-doped carbon was evaluated under similar conditions. The comparison of the linear sweep voltammograms of Fe_3C/C and Fe_3C/NC with those of N–C catalysts is given in Fig. S11.† The comparison between the Fe_3C/C with N–C catalysts demonstrates that the N-doped carbon (N–C) catalysts (without Fe_3C) show better E_{onset}, $E_{1/2}$ and j_{DL} values. The results indicate that Fe_3C is not the only reason for the improved ORR activity of Fe_3C/NC. The superior activity of Fe_3C/NC catalysts can be rationalized by the synergistic effect between the Fe_3C and N-doping active sites. Nevertheless, heating Fe_3C/C with nitrogen precursors can lead to formation of Fe–N$_x$ species, popularly known as active sites

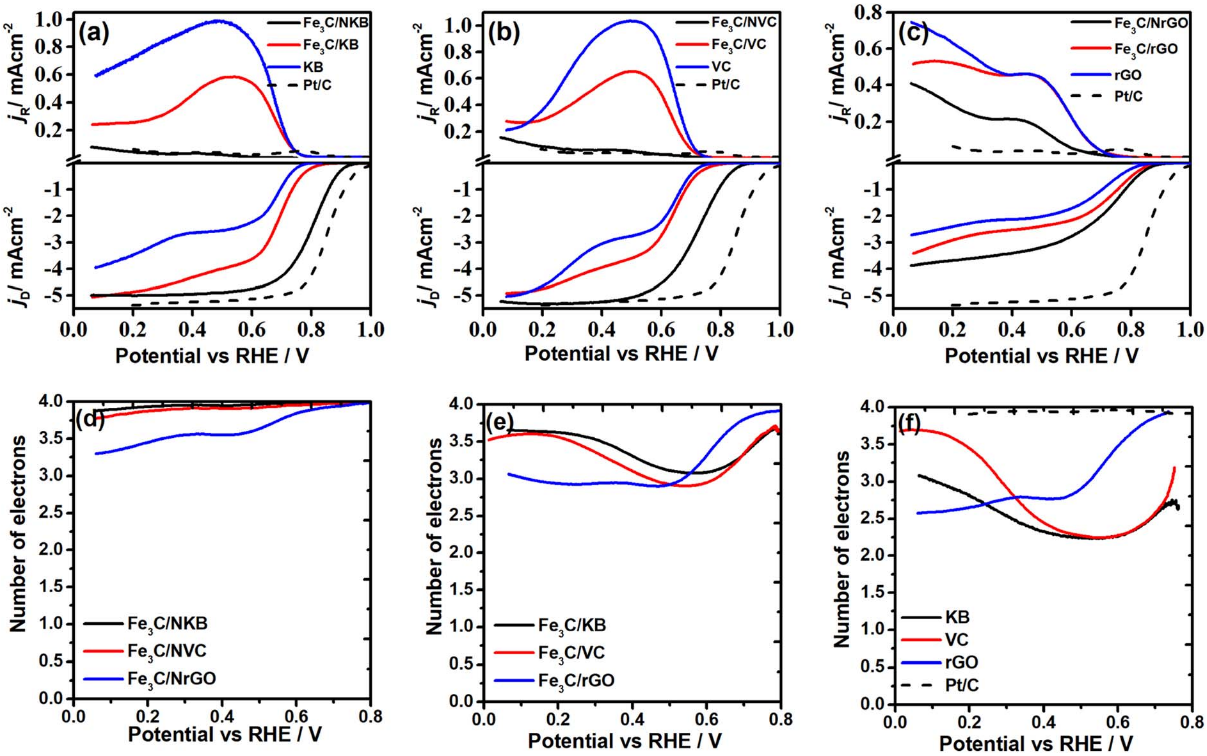

Fig. 5 RRDE voltammograms of the ORR on a pure carbon substrate, bare carbon support, and Fe_3C/C and Fe_3C/NC material (a–c) coated GC electrode in O_2-saturated 0.1 M KOH electrolyte at a scan rate of 10 mV s^{-1}. The dotted line represents the benchmark Pt/C catalysts (loading density 20 μg$_{\text{Pt}}$ cm^{-2}). The ring potential was kept at 1.2 V, and the electrode rotational speed was 1600 rpm. The number of electrons estimated from the ring and disk currents with applied potential on (d) Fe_3C/NC, (e) Fe_3C/C and (f) carbon supports with the benchmark Pt/C catalyst.

for the ORR. These Fe–N_x active sites can form only on the surface of Fe_3C particles in smaller quantities and are very difficult to analyse quantitatively by XPS. Detailed mechanistic studies may help define the active sites and role of Fe_3C in the ORR activity. The ORR activity of Fe_3C/NC catalysts is compared with that of the benchmark Pt/C catalysts, coated on the glassy carbon disk of the RRDE with a loading density of 20 μg_{Pt} cm^{-2}. The Pt/C catalysts show E_{onset} and $E_{1/2}$ potentials of 0.99 and 0.86 V, respectively, which are 30 (in E_{onset}) and 60 mV (in $E_{1/2}$) more positive compared to those of the best performing Fe_3C/NKB catalyst.

3.3 Kinetic & mechanistic analysis

The ORR mechanistic analysis shed some light on the various active sites responsible for the 2-electron and 4-electron ORR. The distinction between 2-electron and 4-electron active sites implies the critical roles of individual species in the catalysts. The elementary kinetic model proposed by Damjanovic *et al.*[49] can be used to calculate the rate constants, followed by the mechanistic analysis, as shown in Scheme 1.

The mass-balanced O_2 and HO_2^- equations from the above kinetic model (Scheme 1) and disk and ring current equations are used to estimate the individual rate constants (see the ESI†).[50,51] The O_2 can be reduced to OH in a direct or indirect (peroxide) pathway. The direct reduction rate constant is referred to as k_1, whereas k_2 (O_2 to HO_2^-) and k_3 (HO_2^- to OH^-) indicate the peroxide pathway rate constants. The estimated individual rate constants for Fe_3C/C are shown in Fig. 6. Similarly, the rate constants of the bare carbon supports were estimated to study the role of Fe_3C (Fig. S12†). The rate constant of O_2 to HO_2^- (k_2) is higher than k_1 (O_2 to OH^-) on the carbon supports, indicating that the carbon supports facilitate the partial reduction of O_2. However, Fe_3C/C shows higher k_1 values indicating improved kinetics *via* the 4-electron pathway.[52,53] The increase in k_1 values is more significant in the lower applied potential region (<0.4 V for Fe_3C/KB and Fe_3C/VC), demonstrating the need for a higher overpotential for the complete 4-electron ORR. Fe_3C/rGO does not show any improved 4-electron reduction activity at higher applied potentials, perhaps due to the nature of the carbon substrate. The k_1 value of Fe_3C/C is 2–3 times higher than that of the bare carbon supports and it is more prominent for Fe_3C/KB. This may be attributed to that KB could be a better host for the Fe_3C particles due to its higher surface area and porous nature, which effectively retains Fe_3C in pores. The carbon supports in Fe_3C/C materials can catalyse the 2-electron ORR, indicated by smaller k_2 values. Based on the rate constants, the ORR activity can be arranged as Fe_3C/KB > Fe_3C/VC > Fe_3C/rGO.

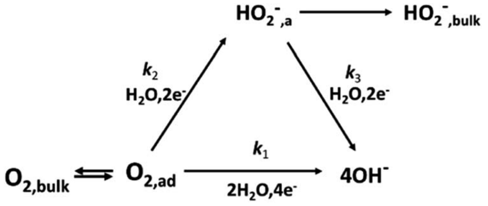

Scheme 1 Kinetic model of the oxygen reduction reaction proposed by Damjanovic *et al.* k_1, k_2 and k_3 are the rate constants. 'ad' refers to the adsorbed species.

The presence of a heteroatom (N-doping) on the Fe_3C/C composite (Fe_3C/NC) brought about significant changes in the ORR kinetics. The estimated rate constants of Fe_3C/NC compared to those of Fe_3C/C are shown in Fig. 7. Fe_3C/NKB exhibits the highest activity with a significant increase in the k_1 values even at more positive potential (lower overpotential region). Although Fe_3C/NVC shows a similar trend as the Fe_3C/NKB, the k_2 values are increasing with potential at the higher overpotential region. The notable increase in the k_1 values suggests that the heteroatom (nitrogen)-doping on Fe_3C/C promotes the entire reduction reaction *via* the 4-electron pathway at lower overpotentials. Although Fe_3C/NrGO shows a similar trend, the k_1 values are smaller than those of the other carbon supports. Conversely, the k_2 values of Fe_3C/NC decrease at lower overpotentials (>0.4 V) compared with those of Fe_3C/C, indicating a decrease in the 2-electron active sites. At higher overpotentials (<0.4 V), the k_2 value shows an increasing trend. The moderate increase in the 4-electron active sites from the

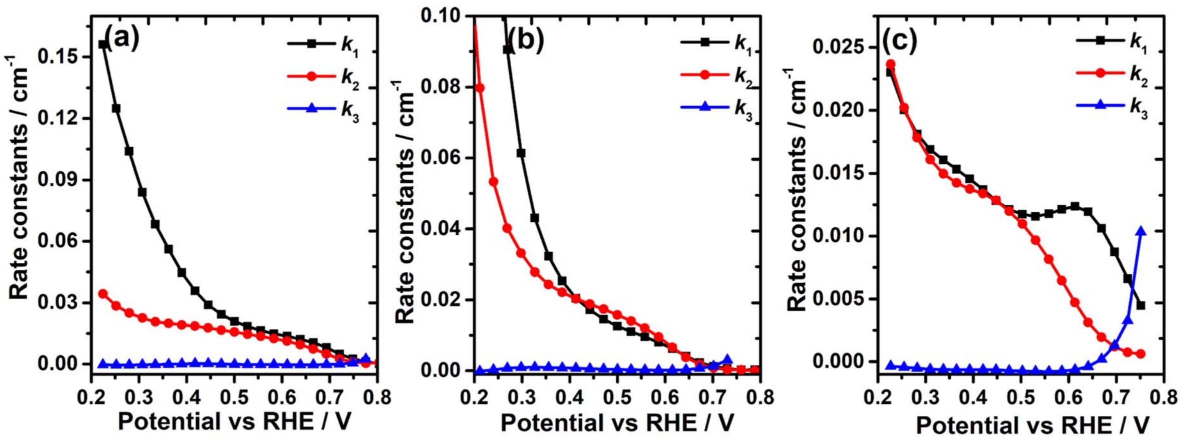

Fig. 6 Potential dependent rate constants of the ORR on (a) Fe_3C/KB, (b) Fe_3C/VC and (c) Fe_3C/rGO composites.

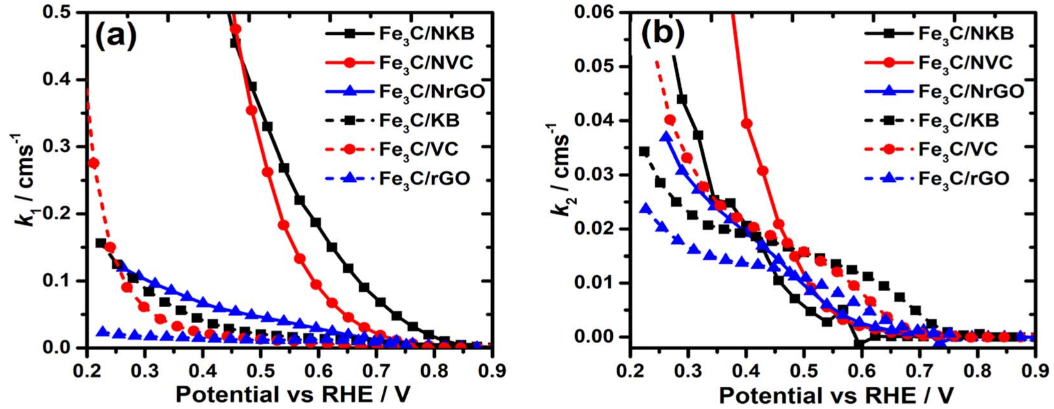

Fig. 7 Potential dependent rate constants (a) k_1 and (b) k_2 of the Fe_3C/NC (solid lines) and Fe_3C/C (dashed lines) catalysts.

bare carbon to Fe_3C/C and a significant improvement were observed while doping with nitrogen (Fe_3C/NC), indicating the formation of 4-electron active sites from bare carbon to Fe_3C/NC.

The durability of the catalysts was examined using the accelerated durability test as explained in the Experimental section. The linear sweep rotating disk electrode voltammograms of the ORR on Fe_3C/NC catalysts before and after the 10 000 cycles of ADT are shown in Fig. 8. The $E_{1/2}$ was taken to study the stability of the catalysts. The negative shift in the $E_{1/2}$ values was observed in all three catalysts. Fe_3C/NVC shows high stability among the catalysts studied with a 30 mV negative shift, followed by Fe_3C/NKB (40 mV). Fe_3C/NrGO shows the least stability with a 120 mV negative shift. The j_{DL} shows a little decrease after the durability test for Fe_3C/NKB and Fe_3C/NVC. However, the decrease in the j_{DL} is significant in the case of Fe_3C/NrGO.

3.4 Zinc–air battery testing

A rechargeable zinc–air liquid electrolyte battery was assembled to evaluate the performance of Fe_3C/NC catalysts. Based on the previous reports, Fe_3C and N–C sites were assumed to be OER and ORR active sites, respectively.[19] A Zn plate (0.5 mm thickness) and catalyst-coated carbon paper (with a loading density of 1 mg cm^{-2}) were used as the anode and cathode, respectively. The electrodes were placed 1.5 cm apart, and the cell was filled with 6 M KOH + 0.2 M zinc acetate electrolyte.[54]

Discharge polarisation experiments were performed using chronopotentiometry (from zero to 300 mA cm^{-2}), as shown in Fig. 9a. The highest positive open circuit potential (OCP) was observed (>1.5 V) for Fe_3C/NC (Fig. S13†). Fe_3C/NVC exhibits higher power density than the other two Fe_3C/NC materials, whereas Fe_3C/NrGO shows the lowest values among the three materials studied. The specific capacity of the Fe_3C/NC compounds was estimated from the chronopotentiometry experiment with a constant discharge current density of 20 mA cm^{-2} (Fig. 9b). The specific capacity varied from 650 to 750 mA h g_{Zn}^{-1}. The results obtained from the zinc–air battery testing are shown in Table 2. The charging–discharging profiles at various current densities are shown in Fig. 9c.

Fe_3C/NVC shows excellent efficiency. The efficiency of the zinc–air battery was calculated from continuous galvanostatic charge–discharging (GCD) experiments (10 minutes of charging and 10 minutes of discharging with continuous 100 hours of

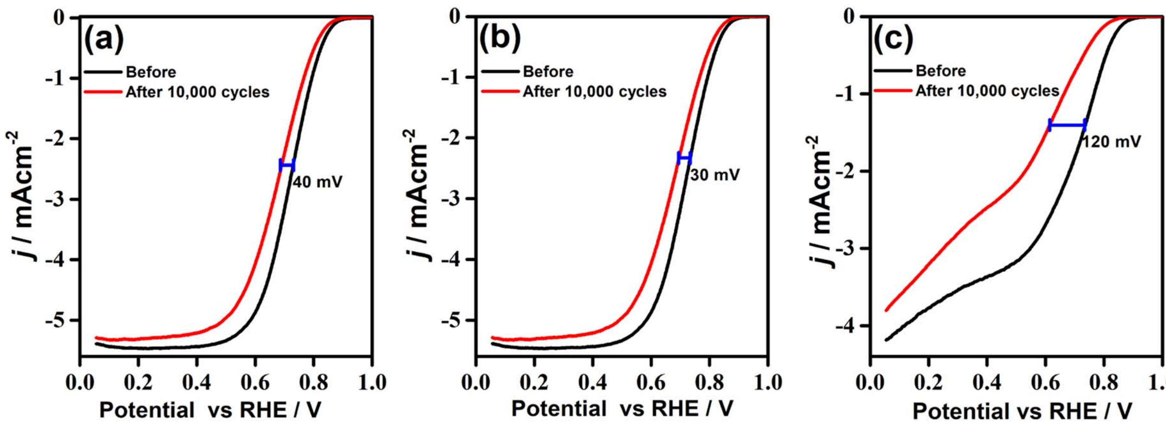

Fig. 8 The linear sweep voltammograms of the ORR on (a) Fe_3C/NKB, (b) Fe_3C/NVC and (c) Fe_3C/NrGO catalysts in O_2-saturated 0.1 M KOH electrolyte. The electrode rotational speed is 1600 rpm and the scan rate is 10 mV s^{-1}. The black and red lines indicate before and after the durability test.

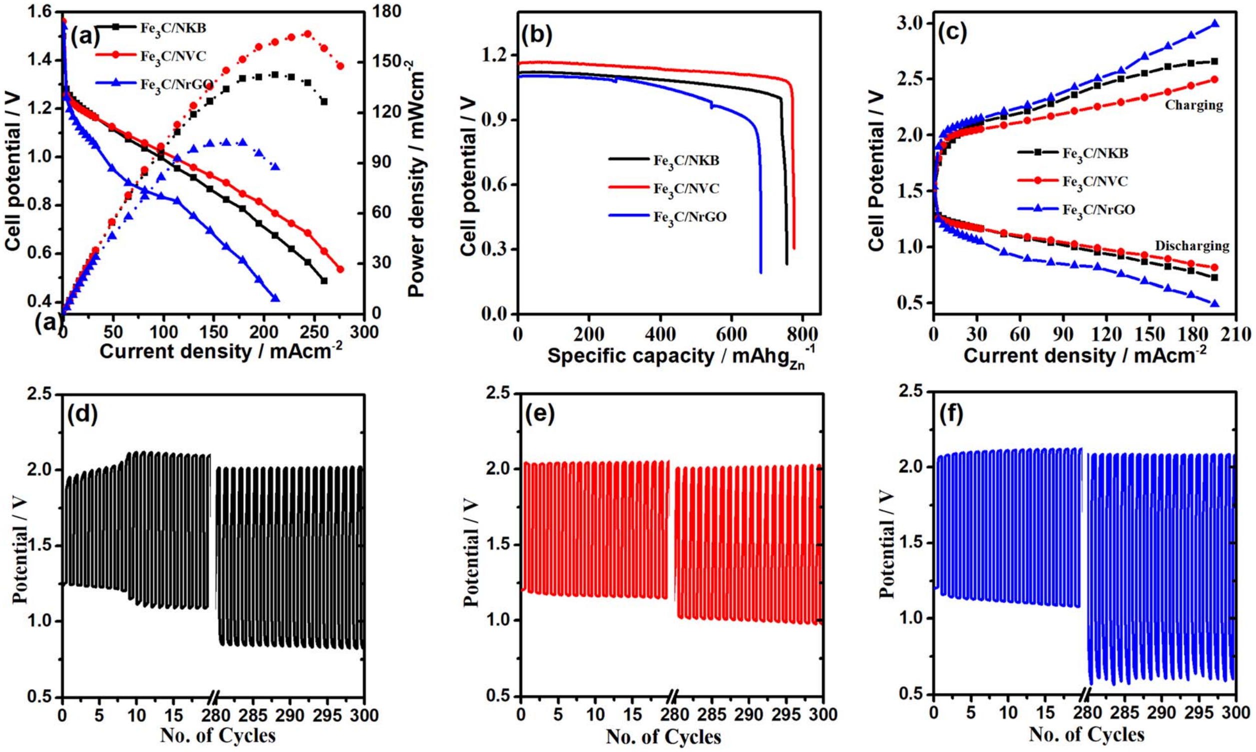

Fig. 9 (a) Discharge polarisation curves, (b) discharge profiles at a constant current of 20 mA cm^{-2} and (c) charging and discharging profiles of Fe_3C/NC materials. The galvanostatic charge–discharge cycles of (d) Fe_3C/NKB, (e) Fe_3C/NVC and (f) Fe_3C/NrGO. Only the initial and final 20 cycles are shown here.

operation) for 300 cycles with a current density of 5 mA cm^{-2}. The efficiency was calculated from the ratio of the potential window of the initial cycle (in the 10th cycle) to the final cycle (300th cycle). Fig. 9d–f show the first and last 20 charge–discharge cycles of the Fe_3C/NC catalysts. Fe_3C/NVC is found to be very stable for 300 cycles with an efficiency of 88%. This may be attributed to the lower Fe content (2.6 wt%) compared with the other materials (12 and 34 wt% in Fe_3C/NKB and Fe_3C/NrGO, respectively) Passivation and leaching could be possible reasons for deactivation of the catalytic activity in Fe_3C/NKB and Fe_3C/NrGO materials. The individual roles of Fe_3C and N-doped carbon/Fe–N can be evaluated based on the cycling performance, *i.e.*, GCD experiments. Fe_3C/NC materials show stable OER potential, and the charging potential did not increase even after 300 cycles. This can be rationalised from previous reports that Fe_3C sites facilitate the OER activity. Conversely, the ORR overpotential increased (more than 200 mV) compared with the initial cycle (Fig. S16†), indicating that ORR activity decreases over a period of time. Therefore the bifunctional activity of Fe_3C/NC catalysts OER and ORR activity originates from Fe_3C and N–C/Fe–N, respectively.

To evaluate the bifunctional activity of Fe_3C/NVC, control experiments were carried out with the Fe_3C/VC and NVC catalysts. Both of them (Fe_3C/VC and NVC) result in much lower power density and specific capacity values than Fe_3C/NVC. The GCD experiments indicate that the Fe_3C/VC catalysts are not stable for more than 230 cycles and the NVC catalysts are stable until 300 cycles. Despite its stability, the NVC catalyst showed lower efficiency than the Fe_3C/NVC catalyst. The benchmark ORR and OER catalysts were used to study the comparative performance of the zinc–air battery. Pt/C and Ir/C (1 : 1) were mixed to prepare the catalytic ink and coated under the similar conditions

Table 2 Zinc–air battery performance parameters of various Fe_3C/NC materials

Compounds	OCP (V)	Power density (mW cm^{-2})	Current density[a] (mA cm^{-2})	Specific capacity[b] (mA h g_{Zn}^{-1})	Efficiency[c]
Fe_3C/NKB	1.50	142	211	738	79%
Fe_3C/NVC	1.56	167	243	756	88%
Fe_3C/NrGO	1.54	102	179	663	58%
Pt/C + Ir/C	1.44	154	244	729	62%

[a] Current density at a maximum power density. [b] Specific capacity is estimated with a constant discharge current of 20 mA cm^{-2}. [c] The efficiency was calculated from the 10th cycle to the 300th cycle (after 100 hours of continuous charging and discharging) difference with a charging and discharging current of 5 mA cm^{-2} where 10 minutes for charging and 10 minutes are for discharging.

described earlier. The power density value is 154 mW cm^{-2} less than that of the Fe_3C/NVC catalyst. The specific capacity and the GCD experiments indicate that Fe_3C/NVC and Fe_3C/NKB catalysts perform much better than benchmark catalysts. After the GCD cycles, the benchmark catalysts show poor performance in OER and ORR regions, indicating the superior bifunctional activity of Fe_3C/NVC. The performance of the Pt/C + RuO_2 (1 : 1) catalysts was also used to compare the literature values. The discharge polarisation curves, specific capacity, and stability tests are given in the ESI (Fig. S13 to S17†).

3.5 Discussion

The N-doping on the Fe_3C/C composites led to improved ORR and OER activity. From the RRDE voltammograms and kinetic analysis, it was found that Fe_3C facilitates the ORR activity *via* the 4-electron pathway. Similarly, the nitrogen-doped carbon (NC) materials exhibit higher ORR activity than both bare carbon and Fe_3C/C materials. Hence the superior ORR activity of Fe_3C/NC catalysts can be defined by the synergy between Fe_3C/C and nitrogen-doped carbon sites.[23,30] The mechanism of the synergistic effect is not yet understood and it can be visualised either by the simultaneous involvement of the two active sites during the adsorption step or the involvement of individual active sites at different parts of the reactions to facilitate and sometimes both.[55] However, the possibility of the formation of Fe–N_x active sites on the surface of Fe_3C particles during the pyrolysis of Fe_3C with nitrogen precursors cannot be eliminated. The kinetic analysis indicates that a significant increase in the direct 4-electron reduction rate constant (k_1) of the ORR on Fe_3C/NC supports the formation of Fe–N_x. XPS cannot detect the Fe–N sites, perhaps due to the smaller content. Furthermore, the ORR activity of the physical mixture of the Fe_3C/C and NC materials was analysed to evaluate the synergistic effect and the importance of Fe–N_x active sites. The physical mixture of Fe_3C/C and NC compounds does not contain any Fe–N_x active sites but consists of Fe_3C and N–C active sites. The ORR activity of such physical mixture catalysts exhibits less ORR activity than individual catalysts such as Fe_3C/C, NC and Fe_3C/NC. This indicates the role of Fe–N_x in the ORR activity. On the other side, the Fe_3C active sites contribute to the OER activity.[19,37,56] The OER potential did not increase even after 300 charge–discharge cycles (100 hours), indicating that the materials are very stable for the OER irrespective of the supporting carbon materials. Fe_3C active sites could be the OER active sites, irrespective of the type of carbon support and nitrogen content. Nevertheless, the role of Fe–N_x in the OER cannot be neglected. The higher stability of Fe_3C/NVC catalysts can be seen from the lower Fe content (2 wt%). Higher Fe content materials are susceptible to passivation and leaching, deactivating the catalytic activity. Finally, the ORR and OER are catalysed by Fe–N_x and Fe_3C sites, respectively.

4. Conclusions

The role of Fe_3C in Fe_3C incorporated nitrogen-doped carbon materials was studied on various carbon supports of different porosities. The PB–carbon (KB, VC, and rGO) composites were pyrolysed in an inert atmosphere, leading to Fe_3C/C. The following conclusions were drawn after the series of half-cell, kinetic analysis and zinc–air battery experiments to define the role of Fe_3C.

Fe_3C/C shows improved ORR activity compared with the bare carbon supports. Besides the positive shift in E_{onset} and $E_{1/2}$ values, the kinetics analysis demonstrates the increasing rate constants of direct 4-electron reduction. This implies the generation of 4-electron active sites due to the introduction of Fe_3C on carbon supports.

The heteroatom (nitrogen)-doping on Fe_3C/C exhibits superior activity, which may be attributed to the synergistic effect of Fe_3C and N–C active sites or Fe–N_x sites. The kinetic analysis demonstrates that the direct 4-electron reduction rate constants increased even at more positive potentials, supporting the formation of Fe–N_x active sites.

The zinc–air battery shows excellent performance while using Fe_3C/NVC as the OER and ORR catalyst. The highest positive OCP (1.56 V) and specific capacity (756 mA h $g_{\text{Zn}}{}^{-1}$) with a power density of 167 mW cm^{-2} were obtained, which is higher than that of the benchmark catalyst Pt/C + Ir/C (1 : 1). Besides, Fe_3C/NVC shows an excellent efficiency (88%).

Finally, the Fe_3C and N–C combination and/or Fe–N_x active sites could be responsible for the ORR activity. Fe_3C/NVC consists of lower Fe content that shows higher stability. The Fe_3C active sites are facilitating the OER. Hence the materials consisting of Fe_3C, N–C and Fe–N_x act as excellent bifunctional catalysts for rechargeable zinc–air batteries.

Author contributions

S. A. G. performed the synthesis, characterisation of materials and electrochemical experiments. A. N. E. performed all zinc–air battery experiments. A. M. designed, supervised and wrote the manuscript.

Conflicts of interest

There are no conflicts to declare.

Acknowledgements

SA thanks CSIR (UGC), India for a fellowship. We thank IISER for the facilities. The authors thank LION Specialty Chemical Co., Ltd., for the carbon samples. Also, the authors thank the reviewers for their enlightening comments on revising the manuscript.

Notes and references

1 X. Hu, S. Chen, L. Chen, Y. Tian, S. Yao, Z. Lu, X. Zhang and Z. Zhou, *J. Am. Chem. Soc.*, 2022, **144**, 18144–18152.
2 Y. Jia, L. Zhang, L. Zhuang, H. Liu, X. Yan, X. Wang, J. Liu, J. Wang, Y. Zheng, Z. Xiao, E. Taran, J. Chen, D. Yang, Z. Zhu, S. Wang, L. Dai and X. Yao, *Nat. Catal.*, 2019, **2**, 688–695.

3 Y. Chen, I. Matanovic, E. Weiler, P. Atanassov and K. Artyushkova, *ACS Appl. Energy Mater.*, 2018, **1**, 5948–5953.

4 K. Artyushkova, A. Serov, S. Rojas-Carbonell and P. Atanassov, *J. Phys. Chem. C*, 2015, **119**, 25917–25928.

5 U. Tylus, Q. Jia, K. Strickland, N. Ramaswamy, A. Serov, P. Atanassov and S. Mukerjee, *J. Phys. Chem. C*, 2014, **118**, 8999–9008.

6 W. Li, J. Wu, D. C. Higgins, J.-Y. Choi and Z. Chen, *ACS Catal.*, 2012, **2**, 2761–2768.

7 C. V. Rao, C. R. Cabrera and Y. Ishikawa, *J. Phys. Chem. Lett.*, 2010, **1**, 2622–2627.

8 T. Ikeda, M. Boero, S.-F. Huang, K. Terakura, M. Oshima and J.-i. Ozaki, *J. Phys. Chem. C*, 2008, **112**, 14706–14709.

9 M. Lefevre, J. P. Dodelet and P. Bertrand, *J. Phys. Chem. B*, 2002, **106**, 8705–8713.

10 C.-X. Zhao, D. Ren, J. Wang, J.-N. Liu, C. Tang, X. Chen, B.-Q. Li and Q. Zhang, *J. Energy Chem.*, 2022, **73**, 478–484.

11 L. Peng, J. Yang, Y. Yang, F. Qian, Q. Wang, D. Sun-Waterhouse, L. Shang, T. Zhang and G. I. N. Waterhouse, *Adv. Mater.*, 2022, **34**, 2202544.

12 X. Xie, L. Shang, X. Xiong, R. Shi and T. Zhang, *Adv. Energy Mater.*, 2022, **12**, 2102688.

13 Y. Wang, L. Wang, Y. Xie, M. M. Tong, C. G. Tian and H. G. Fu, *ACS Sustainable Chem. Eng.*, 2022, **10**, 3346–3354.

14 Z. X. Cao, J. Y. Jia, H. H. Li, Y. H. Wang, X. X. Mao, Z. N. Zhang, M. G. Yang and S. T. Yang, *Int. J. Hydrogen Energy*, 2020, **45**, 3930–3939.

15 X. X. Yang, X. L. Hu, X. L. Wang, W. Fu, X. Q. He and T. Asefa, *J. Electroanal. Chem.*, 2018, **823**, 755–764.

16 Y. L. Niu, X. Q. Huang and W. H. Hu, *J. Power Sources*, 2016, **332**, 305–311.

17 G. K. Wang, W. L. Wang, Y. Chen, C. L. Yan and Z. Y. Gao, *Appl. Surf. Sci.*, 2023, **610**, 155456.

18 Z. Y. Han, W. F. Cai, S. F. Zhao, Y. Zhao, J. R. Bai, Q. Y. Chen and Y. H. Wang, *Nanoscale*, 2022, **14**, 18157–18166.

19 M. Cao, Y. Liu, K. Sun, H. Li, X. Lin, P. Zhang, L. Zhou, A. Wang, S. Mehdi, X. Wu, J. Jiang and B. Li, *Small*, 2022, **18**, 2202014.

20 B. H. Zhang, J. Chen, H. H. Guo, M. Y. Le, H. Z. Guo, Z. Y. Li and L. Wang, *ACS Appl. Nano Mater.*, 2021, **4**, 8360–8367.

21 S. A. Abbas, D. Seo, H. Jung, Y. J. Lim, A. Mehmood and K. M. Nam, *Appl. Surf. Sci.*, 2021, **551**, 149445.

22 W. X. She, Q. R. Xie, Y. H. Huang, C. Y. Xie, X. Y. Zhang, M. C. Sun, F. Wang and J. W. Xiao, *ACS Appl. Mater. Interfaces*, 2020, **12**, 28065–28074.

23 L. L. Cui, Q. L. Zhang and X. Q. He, *J. Electroanal. Chem.*, 2020, **871**, 114316.

24 Z. Y. Wu, X. X. Xu, B. C. Hu, H. W. Liang, Y. Lin, L. F. Chen and S. H. Yu, *Angew. Chem., Int. Ed.*, 2015, **54**, 8179–8183.

25 H. L. Jiang, Y. F. Yao, Y. H. Zhu, Y. Y. Liu, Y. H. Su, X. L. Yang and C. Z. Li, *ACS Appl. Mater. Interfaces*, 2015, **7**, 21511–21520.

26 H. Xu, C. Zhang, Z. Wang, S. Pang, X. Zhou, Z. Zhang and G. Cui, *J. Mater. Chem. A*, 2014, **2**, 4676–4681.

27 Z. Chen, X. M. Gao, X. R. Wei, X. X. Wang, Y. G. Li, T. Wu, J. Guo, Q. F. Gu, W. D. Wu, X. D. Chen, Z. X. Wu and D. Y. Zhao, *Carbon*, 2017, **121**, 143–153.

28 Y. Hu, J. O. Jensen, W. Zhang, L. N. Cleemann, W. Xing, N. J. Bjerrum and Q. F. Li, *Angew. Chem., Int. Ed.*, 2014, **53**, 3675–3679.

29 W. J. Jiang, L. Gu, L. Li, Y. Zhang, X. Zhang, L. J. Zhang, J. Q. Wang, J. S. Hu, Z. D. Wei and L. J. Wan, *J. Am. Chem. Soc.*, 2016, **138**, 3570–3578.

30 X. H. Yan, P. Prabhu, H. Xu, Z. Meng, T. Xue and J. M. Lee, *Small Methods*, 2019, **4**, 1900575.

31 X. R. Zhang, D. D. Lyu, Y. B. Mollamahale, F. Yu, M. Qing, S. B. Yin, X. Y. Zhang, Z. Q. Tian and P. K. Shen, *Electrochim. Acta*, 2018, **281**, 502–509.

32 Y. Zhang, W. J. Jiang, L. Guo, X. Zhang, J. S. Hu, Z. D. Wei and L. J. Wan, *ACS Appl. Mater. Interfaces*, 2015, **7**, 11508–11515.

33 G. Y. Zhong, H. J. Wang, H. Yu and F. Peng, *J. Power Sources*, 2015, **286**, 495–503.

34 J. H. Kim, Y. J. Sa, H. Y. Jeong and S. H. Joo, *ACS Appl. Mater. Interfaces*, 2017, **9**, 9567–9575.

35 R. Venegas, C. Zuniga, J. H. Zagal, A. Toro-Labbe, J. F. Marco, N. Menendez, K. Munoz-Becerra and F. J. Recio, *ChemElectroChem*, 2022, **9**, 20220011.

36 B. K. Barman and K. K. Nanda, *Green Chem.*, 2016, **18**, 427–432.

37 Z. Peng, H. T. Wang, X. C. Xia, X. X. Zhang and Z. H. Dong, *ACS Sustainable Chem. Eng.*, 2020, **8**, 9009–9016.

38 Y. Y. Qiao, P. F. Yuan, Y. F. Hu, J. N. Zhang, S. C. Mu, J. H. Zhou, H. Li, H. C. Xia, J. He and Q. Xu, *Adv. Mater.*, 2018, **30**, 1804504.

39 W. S. Hummers and R. E. Offeman, *J. Am. Chem. Soc.*, 1958, **80**, 1339.

40 A. N. Eledath, A. E. Poulose and A. Muthukrishnan, *ACS Appl. Nano Mater.*, 2022, **5**, 10528–10536.

41 J. Anjana and A. Muthukrishnan, *Catal. Sci. Technol.*, 2022, **12**, 6246–6255.

42 P. Rao, J. Luo, J. Li, W. Huang, W. Sun, Q. Chen, C. Jia, Z. Liu, P. Deng, Y. Shen and X. Tian, *Carbon Energy*, 2022, **4**, 1003–1010.

43 S. Arya Gopal, A. Edathiparambil Poulose, C. Sudakar and A. Muthukrishnan, *ACS Appl. Mater. Interfaces*, 2021, **13**, 44195–44206.

44 G. Liu, X. Li, P. Ganesan and B. N. Popov, *Electrochim. Acta*, 2010, **55**, 2853–2858.

45 Q. Lv, W. Si, J. He, L. Sun, C. Zhang, N. Wang, Z. Yang, X. Li, X. Wang, W. Deng, Y. Long, C. Huang and Y. Li, *Nat. Commun.*, 2018, **9**, 3376.

46 T. Soboleva, X. Zhao, K. Malek, Z. Xie, T. Navessin and S. Holdcroft, *ACS Appl. Mater. Interfaces*, 2010, **2**, 375–384.

47 H. B. Tan, Y. Q. Li, J. Kim, T. Takei, Z. L. Wang, X. T. Xu, J. Wang, Y. Bando, Y. M. Kang, J. Tang and Y. Yamauchi, *Adv. Sci.*, 2018, **5**, 1800120.

48 A. Gabe, R. Ruiz-Rosas, C. González-Gaitán, E. Morallón and D. Cazorla-Amorós, *J. Power Sources*, 2019, **412**, 451–464.

49 A. Damjanovic, M. A. Genshaw and J. O. M. Bockris, *J. Chem. Phys.*, 1966, **45**, 4057–4059.

50 K. L. Hsueh, D. T. Chin and S. Srinivasan, *J. Electroanal. Chem.*, 1983, **153**, 79–95.

51 A. Muthukrishnan, Y. Nabae, T. Hayakawa, T. Okajima and T. Ohsaka, *Catal. Sci. Technol.*, 2015, **5**, 475–483.

52 A. Muthukrishnan and Y. Nabae, *J. Phys. Chem. C*, 2016, **120**, 22515–22525.

53 A. Muthukrishnan, Y. Nabae, T. Okajima and T. Ohsaka, *ACS Catal.*, 2015, **5**, 5194–5202.

54 C.-X. Zhao, J.-N. Liu, B.-Q. Li, D. Ren, X. Chen, J. Yu and Q. Zhang, *Adv. Funct. Mater.*, 2020, **30**, 2003619.

55 E. A. A. Nazer and A. Muthukrishnan, *Catal. Sci. Technol.*, 2020, **10**, 6659–6668.

56 C. Lin, X. Li, S. S. Shinde, D.-H. Kim, X. Song, H. Zhang and J.-H. Lee, *ACS Appl. Energy Mater.*, 2019, **2**, 1747–1755.